Hindcasting and forecasting marsh ecomorphodynamics by integration of model with stratigraphic record

G. Mariotti[1,2]

[1]*College of the Coast and Environment, Louisiana State University, Baton Rouge, LA, USA*

[2]*Center for Computation and Technology, Louisiana State University, Baton Rouge, LA, USA*

Marsh morphodynamics models are usually calibrated using sparse short-term measurements. Hence, their ability to predict long-term trajectories (centuries to millennia) is highly uncertain. Here we improved an existing model for marsh ecomorphodynamics and we used it to hindcast the whole morphodynamic trajectory (2500 years) of an actual salt marsh in New England (USA). The model includes enough processes – among which tidal currents and waves, sand and mud transport, and vegetation population dynamics – to simulate a realistic marsh analogue that closely matches the modern topobathymetry and stratigraphy. Marsh trajectory is highly sensitive to initial bathymetry, mud supply from the nearshore, wave erosion processes, and vegetation dynamics. Each one of these factors is important yet difficult to calibrate on its own. Matching the long-term evolution with the stratigraphic record provides a global constraint for the processes and parameters in the model, increasing the confidence in future long-term predictions. This type of comparison complements those made at short times scales, and it should be used more routinely.

1. Introduction

Coastal marshes started to form 3 to 5 thousand years ago (Braswell et al., 2020) when sea level rise slowed down from ~20 mm/yr to about 1 mm/yr. How exactly this process took place, however, is not well constrained. Indeed, the stratigraphic record provides only sparse information (Braswell et al., 2020; Kirwan and Murray, 2012), and qualitative models are used to reconstruct the marsh trajectory (Redfield, 1972, 1965).

Historical maps have been used to roughly delineate marshes from the 1500s in Europe (Schrijvershof et al., 2021) and from the 1700s in the USA (Bromberg and Bertness, 2005; Priestas et al., 2012). High-resolution historical maps have been used to reconstruct marsh edge erosion since the late 1800s and early 1900s (Burns et al., 2020; Elsey-Quirk et al., 2019; Valentine and Mariotti, 2019). Despite the appeal of these maps, their uncertainty and relatively short time window limit their use. Aerial and satellite imagery provide a more precise reconstruction of marsh dynamics (Gunnell et al., 2013), but they only cover a span of several decades.

Accretion rates over the last century have been measured extensively. Multi-decadal accretion and shallow compaction have been measured with surface elevation tables and feldspar horizons (Cahoon et al., 2019; Doar and Luciano, 2023; Jankowski et al., 2017). Centennial accretion has been measured using cesium and lead radionuclides (Nolte et al., 2013). These data have been extensively used to determine whether the marsh accretion is keeping pace with relative sea level rise (Cahoon et al., 2019; Crosby et al., 2016; Doar and Luciano, 2023; Jankowski et al., 2017), and how accretion is related to tidal range and sediment supply (Coleman et al., 2022). Hence, these data provide a snapshot of the current marsh trajectory, but do not inform about accretion during the early marsh stages and how accretion will change with feedbacks associated with the evolving morphology (which includes not only changes in marsh elevation, but also changes in the channel network and tidal flat). Additionally, there are often large discrepancies between these short-term measurements and millennial scale assessments of marsh stability (Törnqvist et al., 2020) owing to differences in measurement types and the incompleteness of stratigraphic measurements (Törnqvist et al., 2021). Physics based models capable of resolving relevant processes which operate over short timescales but spanning millennial scale marsh evolution could bridge this gap.

Simplified models for marsh accretion have been developed and applied to real marsh sites (Alizad et al., 2022; Craft et al., 2009; Langston et al., 2020; Mariotti et al., 2020), filling the gaps between the sparse field data and providing predictions about future accretion. All of these models, however, assume static channels and tidal flats, and hence neglect the associated morphodynamic feedbacks. Marsh morphodynamic models that include these feedbacks exists, but have mostly been applied to idealized cases, ranging in size from ~1 to 100 km^2. These latter models cannot directly inform the future evolution of a particular marsh, but rather provide general insights.

Marsh morphodynamic models have highlighted the importance of both tidal currents and waves (Carniello et al., 2009; Colina Alonso et al., 2023; Willemsen et al., 2022). In particular, waves control the resuspension on the tidal flat (and hence the possibility for vegetation establishment), and also cause marsh edge retreat (Mariotti and Canestrelli, 2017). Morphodynamic models have highlighted the importance of both sand and mud (Boechat Albernaz et al., 2023; Carniello et al., 2012; Colina Alonso et al., 2023). Sand is generally the underlying substrate, and it is present in the bed of the larger channels as well as in bars in proximity of inlets. Mud blankets the sand substrate, and it is found predominantly on shoals distal from inlets, smaller channels, and in marsh soil (Colina Alonso et al., 2023). Except where a direct riverine input is present, mud supply from the nearshore is a crucial for filling a basin (Mariotti and Canestrelli, 2017). Morphodynamic models have also revealed the dynamics of marsh vegetation establishment and development (Gourgue et al., 2021; Willemsen et al., 2022; Xu et al., 2022). They have identified the importance of both random seeding and lateral plant expansion (Cao et al., 2021). They also pointed out that vegetation can disappear due to both high levels of inundation and high levels of hydrodynamic stress.

Despite their progress, morphodynamic models have not been able to hindcast a real marsh site, that is, recreating the past marsh condition to a degree where a direct comparison with field measurements is possible. Direct comparison with a model that includes marsh dynamics has only been performed at decadal time scale (Brückner et al., 2019; Van Der Wegen et al., 2023). Centennial time scale comparison has only been performed in large estuarine systems, such as the Schelde estuary (Netherlands) (Dam et al., 2016; van der Wegen and Roelvink, 2012) and San Pablo Bay (California, USA) (Elmilady et al., 2019). These models focused mostly on the main channels and tidal flat, and did not include marsh dynamics.

Here we present a marsh evolution model that includes all the relevant morphodynamic mechanisms: tidal currents and wind waves, sand and mud transport, and vegetation population dynamics (which include inundation-dependent carrying capacity, logistic growth, seeding, lateral expansion, and mortality due to hydrodynamic). We then apply the model to a realistic initial bathymetry and boundary conditions, with the goal of recreating a real site. We consider the Barnstable marsh (Massachusetts, USA), which has been the subject of some of the first and more detailed field studies (Redfield, 1972, 1965). We then 1) test the ability of a model to reproduce the whole marsh trajectory by comparing it with the measured stratigraphy, 2) perform a sensitivity analysis with respect to the model parameters, 3) make centennial predictions about the future evolution of the marsh.

2. Methods

MarshMorpho2D is a marsh evolution model that includes a variety of processes (Mariotti, 2020; Mariotti and Finotello, 2024). Several improvements are here introduced to better reproduce hydrodynamics, sediment transport, and vegetation processes, while keeping the model numerically efficient.

2.1.1 Representative tidal flow

The model calculates a tidal flow velocity field $\boldsymbol{U}$=(U_x,U_y), representative of half a tidal cycle (i.e., either the ebb or flood phase), based on a balance between pressure gradient and bed friction, and considering a tide-averaged water depth h for each cell (Mariotti, 2020, 2018). The water depth is calculated as the average between high tide, mid tide, and low tide.

$$h = [\max(0, r/2 + sla - z^*) + \max(0, sla - z^*) + \max(0, -r/2 + sla - z^*)]/3 \quad (Eq. 1)$$

where r is the tidal range, sla is the sea level anomaly, and z is the bed elevation with respect to a fixed datum and z^* is z minus mean sea level. For numerical stability reasons, the minimum water depth is set equal to 1 cm. The continuity and momentum equations read

$$\nabla \cdot (h\boldsymbol{U}) = S \quad (Eq. 2)$$

$$\boldsymbol{U} = \frac{1}{U_o}\frac{h^{4/3}}{n^2}\nabla\eta \quad (Eq. 3)$$

The term η denotes the elevation of the free surface, whereas S is the source term for the tidal prism, equal to $S = [r/2 - \max(-r/2, \min(sla - z^*, -r/2))]/(T/2)$, where T is the tidal period. The value of U_o is initially set equal to 1 m/s, even though any value that is spatially uniform would provide the same solution of Eqs. 2-3 (Mariotti, 2018). The Manning coefficient (n) is dependent on the presence or absence of vegetation.

Eqs. 2-3 are recalculated by with an updated value of U_o,

$$U_o = |\boldsymbol{U}| \ (from\ previous\ iteration) \quad (Eq. 4)$$

If this method was iterated many times, it would converge to solving the original Manning's equation,

$$\boldsymbol{U} = \frac{h^{2/3}}{n}\sqrt{\nabla\eta} \quad (Eq. 5)$$

For the sake of limiting the numerical computation, we instead iterate only one time, and average with a reference velocity U_{ref} (set equal to 1 m/s).

$$U_o = (Uref + |\boldsymbol{U}|(from\ previous\ iteration))/2 \quad (Eq. 6)$$

2.1.2 Shallow tidal flow

The model calculates a reference tidal flow for the whole tidal cycle, assuming a constant (yet spatially variable) water depth. This neglects very shallow flow (Fagherazzi and Mariotti, 2012), which are important to create the fine-scale channel network on the tidal flat. We thus calculate another flow field ($\boldsymbol{U}_s$)

$$\nabla \cdot (h_s \boldsymbol{U_s}) = S_s \quad (Eq. 7)$$

$$\boldsymbol{U_s} \propto \frac{{h_s}^{4/3}}{n^2} \nabla \eta_s \quad (Eq. 8)$$

where we considered the average between the water depth at mid tide and at low tide.

$$h_s = [\max(0, sla - z^*) + \max(0, -r/2 + sla - z^*)]/2 \quad (Eq. 9)$$

And the source term for the tidal prism

$$S_s = \begin{matrix} \frac{1}{N}\frac{r}{T/2}\pi & \qquad -r/2 < z^* < \ 0 \\ 0 & \qquad else \end{matrix} \quad (Eq. 10)$$

The parameter N (here set equal to 10) specifies the fraction of the tidal cycle during which the shallow flow is computed. Assuming a half tidal period of 6.2 hours, this means that the shallow tidal flow is calculated considering a period of about 40 minutes. The factor π is included to simulate a sinusoidal distribution of the tidal velocity.

In order to limit the effect of this flow in large channels, where the shallow flow discharge from a large area might accumulate, the maximum discharge from the shallow flow is limited to Q_{smax} (here set equal to 1 m^2/s),

$$|\boldsymbol{U_s}| = \frac{\min(Q_{smax}, |\boldsymbol{U_s}| h_s)}{h_s} \quad (Eq. 11)$$

2.1.3 Sea waves

Locally generated wind waves (sea waves) are calculated considering different tidal stages. Given a tidal range and sea level anomaly, the water level is considered at equispaced intervals (here set equal to five) from low tide to high tide. The water depth thus reads

$$h_W(t) = \max\left(0, \frac{r}{2} I + sla - z^*\right) \quad (Eq. 12)$$

where I is a vector equispaced from -1 to 1. At each tidal stage a mask is created by considering areas that are not vegetated and have a water depth of at least 0.2 m. Given a wind direction, the fetch is calculated over every cell of the domain. The fetch is then spatially smoothed to avoid sharp discontinuity, approximating wave diffraction and refraction.

At each tidal stage the wave height (H_W) and period (T_W) are calculated based on the local water depth, fetch, and wind speed (Young and Verhagen, 1996). From the wave height and wave period, the wave number (k_W), wave orbital amplitude (a_W), and the wave bottom orbital velocity (u_W) are calculated using the wave linear theory (Wiberg and Sherwood, 2008).

2.2 Dynamic model for vegetation population

The marsh vegetation model considers an equilibrium value for the vegetation biomass, B_{eq}. As in previous models, this value only depends on marsh elevation (Morris et al., 2002), and it ranges from 0 to 1,

$$B_{eq} = \begin{matrix} 4(z^* - z_{lo})(z^* - z_{hi}) & z_{lo} < z^* < z_{hi} \\ 0 & z^* \leq z_{lo} \ or \ z^* \geq z_{hi} \end{matrix} \quad (Eq. 13)$$

where z_{lo}=-0.1 and z_{hi}= MMMHW+0.1m, with the Median Monthly Maximum High Water (MMMHW) calculated based of a ~20 year time series of water levels as in (Mariotti and Zapp, 2022).

Similar to previous models (van de Vijsel et al., 2023), marsh vegetation growth logistically,

$$\frac{dB}{dt} = v_{growth} B(1 - B/B_{eq}) \quad (Eq. 14)$$

with a scale growth rate v_{growth} [yr^{-1}]. Given that the growth rate is zero when the vegetation is zero, an area where the vegetation can be present (i.e., $B_{eq}>0$) but that is initially unvegetated ($B=0$) would remain so. Two processes enable the vegetation to initiate in these areas: seeding and lateral expansion.

Seeding occurs randomly throughout the domain, at a rate v_{seed} [yr^{-1}]. Seeded cells are assigned an initial biomass value B_o (set equal to 0.1). Lateral expansion, which simulates clonal growth, occurs at a constant rate $v_{expansion}$ [m/yr]. In practice, a cell that is adjacent to a vegetated cell becomes vegetated with a probability $v_{expansion} \Delta t / \Delta x$. As for the seeding, the newly vegetated cell is assigned the value B_o.

Finally, vegetation can be destroyed by hydrodynamic stress (Brückner et al., 2019; Willemsen et al., 2022). Here we model this by setting the biomass to zero when the bed shear stress is greater than the critical shear stress for mud resuspension.

For comparison, a previous version of the model (Mariotti, 2020), as well other models (Alizad et al., 2016; D'Alpaos et al., 2012) simply assumed $B=B_{eq}$.

2.3 Sand and mud transport

The model calculates the transport of both mud and sand. All transport is assumed to occur in suspension, through the tidal dispersion mechanism (Di Silvio et al., 2010). This is obtained by solving the steady state balance

$$\nabla \cdot \left((\boldsymbol{K} + K_o) h \nabla \mathrm{c} \right) = D - E \quad (Eq. 15)$$

where c is the sediment concentration of either sand (c_S) or mud (c_M). The coefficient for the tidal dispersion ($\boldsymbol{K}$) reads

$$\begin{aligned} K_x &= k U_x^2 T/2 \\ K_y &= k U_y^2 T/2 \end{aligned} \quad (Eq. 16)$$

where k is a nondimensional factor, set equal to 0.1 for mud and 0.5 for sand. K_o is the baseline diffusivity, representing processes not associated with astro-meteorological tides (e.g., wind driven transport driven by local forcing, wave driven transport, turbulent mixing). This term is only present for mud, and it is equal to 10 m^2/s in unvegetated areas and to 0.1 m^2/s in vegetated areas.

D is the deposition rate (either D_S or D_M)

$$D = wcf \quad (Eq. 17)$$

The settling velocity *w* differs for sand (w_S) and mud (w_M), and it is modified when vegetation is present. *f* is the hydroperiod, which is calculated in a simplified way,

$$f = \min\left[1, \max\left(0, \frac{r}{2} + sla + msl - z\right)/r\right] \quad (Eq. 18)$$

E is the erosion rate from the bed (either E_S or E_M), and it accounts for resuspension by both currents and sea waves.

$$\begin{array}{c} E_S = E_{S\_tialflow} + E_{S\_shallowtialflow} \\ E_M = E_{M\_tialflow} + E_{M\_shallowtialflow} + E_{M\_sea} \end{array} \quad (Eq. 19)$$

To calculate resuspension by tidal current, an empirical sinusoidal modulation of the tidal currents is introduced

$$Ui(t) = |\boldsymbol{U}|\pi sin(2\pi t/(T/2)) \quad (Eq. 20)$$

In order to avoid unrealistic high velocity on the marsh platform, we limit the velocity so that the maximum Froude number is 0.3, that is,

$$Ui = \min\left[Ui, 0.3\sqrt{hg}\right] \quad (Eq. 21)$$

where *g* is the gravity acceleration. This limiter has negligible effect in the channels, where water depths are on the order of meters.

Next, mud resuspension by currents is computed with a modified Partheniades equation (Carniello et al., 2012)

$$E_{M\_tialflow} = m_e \frac{1}{T/2} \int_0^{T/2} \left(\sqrt{1 + ([\rho_w g h^{-1/3} n^2 Ui^2]/\tau_{cr})^2} - 1 \right) dt \quad (Eq. 22)$$

where m_e is the mud erodibility, τ_{cr} is the critical shear stress for mud erosion, and ρ_w is the water density.

Sand resuspension by currents is calculated with the Engelund & Hansen formula averaged over half tidal cycle (Mariotti, 2021)

$$E_{S\_tialflow} = w_s \frac{1}{T/2} \int_0^{T/2} 0.05 \frac{n^3 Ui^4}{h^{1.5} g^{0.5} (\rho_s/\rho_w - 1)^2 d_{50}} dt \quad (Eq. 23)$$

Sand and mud resuspension by shallow tidal flow are calculated in a similar way,

$$E_{M\_shallowtialflow} = \frac{1}{N} m_e \left(\sqrt{1 + \left(\left[\rho_w g {h_s}^{-1/3} n^2 |\boldsymbol{U_s}|^2 \right] / \tau_{cr} \right)^2} - 1 \right) \quad (Eq. 24)$$

$$E_{S\_shallowtialflow} = \frac{1}{N} 0.05 \frac{n^3 |\boldsymbol{U_s}|^4}{{h_s}^{1.5} g^{0.5} (\rho_s/\rho_w - 1)^2 d_{50}} \quad (Eq. 25)$$

where the factor N is included because this flow only takes place for a fraction of the tidal cycle.

Finally, resuspension of mud by sea waves is calculated as

$$E_{sea} = m_e \frac{1}{T/2} \int_0^{T/2} \left(\sqrt{1 + ([0.5 \rho_w f_w(t) (u_w(t))^2]/\tau_{cr})^2} - 1 \right) dt \quad (Eq. 26)$$

where the time represents the different tidal stages described in section 2.1.3, and f_w is a friction factor (Swart, 1974)

$$f_w = min(0.3, 0.00251 exp[5.21 (a_w/d_o)^{-0.19}]) \quad (Eq. 27)$$

where d_o is the bed roughness, set equal to 1 mm.

The erosion and deposition rate are then used to update the sediment thickness, and specifically the thickness of the active layers (Y_s and Y_M),

$$\frac{\partial Y_S}{\partial t} = \frac{D_S - E_S}{\rho_{bulk\_S}} - \nabla \cdot F_S \quad (Eq. 28)$$

$$\frac{\partial Y_M}{\partial t} = \frac{D_M - E_M}{\rho_{bulk\_S}} - \nabla \cdot F_M + O - C \quad (Eq. 29)$$

The downslope flux is calculated proportional to the bed slope. For mud it reads

$$F_M = (\mu + a_M E_{M\_tialflow}) \nabla z \quad (Eq. 30)$$

where μ is equal to 0.1 in unvegetated areas and to 3 in vegetated areas, and a_M is equal to 0.2 (Mariotti, 2020; Mariotti and Finotello, 2024). For sand it reads

$$F_S = \left[a_S E_{S\_tialflow} + \frac{16 e_S C_S \rho_w}{15\pi(\rho_s - \rho_w) g} \frac{1}{w_S} \left(\frac{\pi H_W}{\sqrt{2} T_W \sinh{(k_W h_W)}} \right) \right] \nabla z \quad (Eq. 31)$$

where a_M=5 and where C_s=0.1, e_s=0.1 (Mariotti, 2021; Ortiz and Ashton, 2016). Thus, the effect of wind waves on sand is only to smoothen the bed, and it is not directly coupled to the tidal transport.

The in situ organic accretion is calculated proportional to the vegetation biomass

$$O = R_{org} B \quad (Eq. 32)$$

where R_{org} is the maximum accretion rate. The organic material is added to the mud (Y_M), and it is not tracked as a separate constituent when it gets eroded. *C* is the marsh compaction rate, which is only applied where marsh vegetation is present. Finally, the mean sea level is increased according to the Relative Sea Level Rise rate (*R*).

2.4 Stratigraphy and sand-mud interactions

The stratigraphy is stored in cells with a constant thickness (equal to 0.5 m) and variable ratio of sand and mud. The bed elevation is calculated as the sum of the two active layers (Y_S and Y_M) plus the elevation of the top of the stratigraphy stack. When the active layer becomes smaller than a threshold (0.2 m), the uppermost underlying layer is merged to the active layer; when the active layer becomes larger than a threshold (0.8 m), it is split and the lower portion is added on top of the underlying stratigraphy.

The erosion of sand and mud mixtures has been extensively studied and parameterized (Le Hir et al., 2011; van Ledden et al., 2004). For sand, experimental studies indicate that the erosion of sand decreases monotonically with the ratio of mud, with a smaller decrease at low mud fraction and a higher decrease at higher mud fraction (Colina Alonso et al., 2023). For simplicity, we assume that the decrease is linear with the mud fraction in the active layer χ_M,

$$\chi_M = \frac{Y_M}{Y_M + Y_S} \quad (Eq. 33)$$

For mud, erosion has a non-monotonic relationship with the mud fraction: it peaks at intermediate values of the mud fraction due to the feedback with bedforms and hence bed roughness (Colina Alonso et al., 2023). For simplicity we assume that mud resuspension is not affected by the mud fraction. In practice this means that mud can always be winnowed away from sand, provided that the hydrodynamics was able to resuspend it were sand not present.

In addition to the limiter based on mud fraction, a limiter is added based on the total sediment availability. In particular, E_s is set equal to zero when $Y_s \leq 0$ and E_M is set equal to zero when $Y_M \leq 0$. Noticeably, both Y_s and Y_M can become slightly smaller than zero during a single morphodynamic step. In that case, this negative amount of material is still kept track of (so that mass is conserved), but the bed elevation is calculated assuming that the active layer thickness is zero. Then, when sediment is eventually added to the layer and the thickness becomes positive, the usual dynamic returns.

Knowledge on how downslope sediment transport is affected by the sand and mud ratio is limited, and hence highly simplified relationships are implemented here. First, the downslope transport of sand and mud is multiplied by the sand and mud fraction, respectively. Second, they are multiplied by a sediment availability factor, $1 - \exp(-10/Y_{S,M})$.

This factor gradually reduces to zero the transport when the thickness of the sand or mud approaches zero and removes unrealistic numerical effects.

2.5 Ponding, wave edge erosion, channel meandering

Other processes are included as previously implemented, and here are only discussed briefly. Wave edge erosion rate (*W*) is calculated as

$$W = a_{edge}Pf \quad (Eq. 34)$$

where the wave power (*P*) is calculated as the average for the various tidal stages (see section 2.1.3), a_{edge} is the marsh edge erodibility, and where the term *f* is included to take into account the reduction in the tide-averaged wave power when the bed is located above MLW, i.e., the bed is dry for some portion of the tidal cycle. The process of marsh edge erosion is numerically implemented using a probabilistic approach (Mariotti and Canestrelli, 2017). The eroded material is redistributed in the nearby cells, and it is completely conserved in the case of sand, while it is partly (25%) removed in the case of mud, simulating the process of organic matter oxidation.

Ponding dynamics include pond formation by random seeding and impoundment, pond lateral expansion and deepening, and pond merging (Mariotti, 2020, 2016). Pond active deepening, which simulated organic matter decomposition, is only implemented on the mud fraction of the sediment (which is assumed to contain all the organic matter).

Channel meandering is implemented in a simplified way. First, the tidal flow $\boldsymbol{U}$ is modified based on the flow curvature (Mariotti and Finotello, 2024), such that the velocity increases in the outer bend and decreases in the inner bend. Second, an additional bank erosion mechanism is calculated as a function of the flow curvature strength at the outer bank (Mariotti and Finotello, 2024).

2.6 Model set up

The model is set up to reproduce the Barnstable marsh (Massachusetts, USA), which has been extensively studied (Redfield, 1972). The marsh has a semidiurnal tide with a mean range of 2.87 m. The marsh has no direct riverine input, and it is located in an area with low anthropogenic disturbances.

The basin is characterized by fine-medium sand, silty mud, and peat (Redfield, 1972). Except for the inlet, where the sand grain size is between 0.5 and 1 mm, the sand grain size in the basin is about 0.1-

0.3 mm. For simplicity, we only consider one sand grain size, equal to 0.25 mm. For mud, we did not specify a size, but rather impose a settling velocity (0.2 mm/s) and a critical shear stress (0.2 Pa). Organic material, once produced, is incorporated into the mud fraction.

We consider a simplified domain bounded by the upland and the barrier island, and open at the inlet. We assumed that the barrier island did not change during the simulated time: stratigraphic record indicate that the barrier has reached the current position about 2500 years ago, and minimal transgression has occurred (van Heteren and van de Plassche, 1997).

We considered a slope in the along-basin direction, and slope in the cross-basin direction (mainly aligned with the cross-continent slope). This was informed by the presence of very old marsh cores in the south (and slightly west) area of the basin. We also consider an initial slope at the edge of the basin. Grid resolution Δx was set equal to 20 m.

We considered time variable tidal range and sea-level anomaly, obtained from the water level measured in Boston (NOAA station 8443970) (Mariotti and Zapp, 2022). Both are assumed to be constant in space, which is reasonable given the short length of the basin (Zapp and Mariotti, 2023). Wind speed and direction was obtained from a nearby NOAA buoy (Mariotti and Zapp, 2022); wind speed was reduced by 15% to account for decrease in wind speed from offshore to sheltered areas (Mariotti et al., 2018). Morphodynamics times steps Δt were set equal to 0.5 years, which is appropriate for these types of simulations (Mariotti and Zapp, 2022).

We included an area near the inlet where waves are artificially imposed, simulating the swell propagating into the basin. The swell height decreases exponentially from a height of 1 m, with an e-folding length of 500 m.

Mud concentration at the inlet was set equal to 10 mg/l, consistent with a relatively low mud supply. Suspended sediment concentrations of about 10 mg/l were measured in the main channels of Barnstable (Mariotti et al., 2020). This concentration represents the equivalent value if the supply was constant – whereas in reality is highly variable in time, and it mostly associated with wave resuspension in the nearshore (Baranes et al., 2022). Sand concentration at the inlet was set equal to 0.2 mg/l, and it was calibrated to obtain a channel depth of about 10 m.

Relative sea level rise was set equal 0.7 mm/yr, matching a precise sea level reconstruction for the last 2500 years (Hein et al., 2010). Shallow peat compaction (*C*) was set equal to 2 mm/yr, in line with measurements of regional marsh compaction in a marsh located about 50 km north of Barnstable, which found a compaction of 30 cm over about 120 years (Yellen et al., 2023). Compaction is held constant in time and applied to all vegetated cells.

Marsh edge erodibility depends in a non-linear way on marsh soil properties. Given the relatively high strength of New England marshes (Houttuijn Bloemendaal et al., 2021), compared for example to those in the Mississippi Delta (Jafari et al., 2019), a low value of marsh erodibility is chosen, equal to 0.01 m/yr/(W/m).

Finally, more than half of the marsh has been ditched since the 1930s, resulting in the drainage of marsh ponds (Mariotti et al., 2020). Here we neglect this process for two reasons. First, ditching only occurred over a short time interval with respect to the whole marsh trajectory. Second, given the relatively coarse spatial resolution (20 m), it would not be possible to directly simulate ditching in the model (but it could be theoretically parameterized as a subgrid drainage).

3. Results

3.1 Recreating present-day topobathymetry and marsh stratigraphy

In the initial phase of the simulation the existing sand substrate is reworked by tidal currents, which incise the channel network (Fig. 2, video 1). Mud imported from the nearshore is deposited toward the edges of the basin, which eventually leads to the establishment of fringing marshes. Marshes also form on isolated sand bars adjacent to channels that dissect the tidal flat (Fig. 2). After about 1500 years most of the basin is filled with marshes. Over the following 1000 years the marsh expands gradually, and at year 2500 both the marsh extent and the topobathymetry is similar to the modern one (Fig. 2).

Marsh ages predicted by the model match the stratigraphic record (Fig. 3). As for the measurements, the oldest marsh (2500 years) predicted by the model is found at the edges of the basin, especially at the southern edge. The model predicts marsh ages of about 1500 years in the middle-west part of the basin, matching measured ages of 1510 and 1535 years. Eastward of this marsh, the model predicts a younger marsh (500-1000 years), which matches measured ages of 544, 625, 850, and 856 years. Finally, the model predicts marsh formation in the middle-south portion of the basin in the last few hundred years, which matches marsh formation reconstructed by historical maps (Fig. 1).

The inner bend marsh progradation associated with channel meandering also creates pockets of younger marsh surrounded by older marsh (Fig. 3). This agrees with unusually young marshes along the main channel (Fig. 3), e.g. those with ages of 610 and 144 years directly adjacent to one another. Given the slow rate of channel migration, however, the effect on the overall marsh age is small.

3.2 Sediment dynamics and marsh accretion

We considered a fixed bathymetry – the simulated present-day configuration at year 2500 – and calculated suspended mud concentration (c_m) with different hydrodynamic forcings (Fig. 4A). Tidal currents associated with the largest tidal range and sea level anomalies creates c_m in the channels on the order of 20 mg/l (Fig. 4), whereas currents associated with the mean tidal range only create c_m of about 5 mg/l. Wind resuspension creates a highly spatially and temporally variable c_m, with peaks on the order of 100s of mg/l, concentrated on the mud shoals facing the marsh edge (Fig. 4A).

For comparison we considered sediment measurements in Plum Island Estuary, which is located about 200 km north and has a similar tidal range and wind regime, and presumably similar sediment dynamics. A field survey in a large tidal channel there reported peak values on the order of 100-300 mg/l for the largest tidal ranges (Fagherazzi et al., 2017). The lower values predicted by our model (about 20 mg/l) can be explained considering that the model calculates a tide-average value, which is an order of magnitude lower than the peak values. Field measurements in the marshes of Plum Island Estuary found values on the order of 0-5 mg/l (Coleman et al., 2020), which is well predicted by the model (Fig. 4A). Finally, values of 5-20 mg/l in the open tidal flat of Plum Island Estuary (Zhang et al., 2020) are also consistent with model predictions.

Vertical accretion is strongly controlled by the marsh elevation. On the higher (and older) marsh platform accretion is dominated by in situ organic production (3-4 mm/yr) (Fig. 4C), whereas mud accretion is about 1 mm/yr (Fig. 4B). Together they roughly match the RSLR plus consolidation rate (3+2=5 mm/yr), and are consistent with marsh vertical accretion rates of about 5 mm/yr measured over the last ~50 year in the high marsh of Barnstable (Mariotti et al., 2020) and Plum Island Estuary (Wilson et al., 2014). On newly formed marsh, which is 0.5 to 1 m lower than the high marsh platform, both in situ organic accretion and mud deposition are on the order of 5 mm/yr. These values also agrees with vertical accretion measurements on the low marsh of Plum Island Estuary on the order of 10 mm/yr (Wilson et al., 2014).

3.3 Sensitivity analysis

To test the sensitivity of the results, we performed morphodynamic simulations as for the reference case (2500 years long, with RSLR acceleration in the last 100 years), but changing one parameter at the time.

With a shallower (+0.3 m) initial bathymetry, the basin fills with marshes only a few percent more than the reference case (Fig. 5). On the other hand, with a deeper (-0.3 m) initial bathymetry, the basin fills less, and has roughly half the marsh extent than the reference scenario (Fig. 5).

With a higher mud supply (c_{Mo}=15 mg/l), the basin completely fills with marshes (Fig. 6). With a lower mud supply (c_{Mo}=5 mg/l) the basin barely fills and has only a small amount of marsh in the southern portion of the basin (Fig. 6).

Morphodynamics is highly sensitive to wind forcing. Reducing the wind speed by 10% increases the net import of sediment and the basin completely fills with marshes, similar to the case with a higher mud supply (Fig. 7). Increasing the wind speed by 10% decreases the net import of sediment and the basin barely fills with marshes, similarly to the case with a lower mud supply. When wind is not included in the model, the basin completely fills with marshes. When wave edge erosion is not included the marsh extent is slightly larger (~10% more) than the reference case, but it does not completely fill in. When wave edge erosion is doubled, the marsh extent is reduced by about 30%. Doubling wave-induced mud bed erosion (Eq. 26) creates a deeper basin and drastically reduces the formation of marshes. In particular, marsh formation is inhibited at the edges of the basin, whereas it is slightly enhanced on sand bars in the seaward portion of the basin.

Increasing the seeding rate (v_{seed}) tenfold increases basin filling, and in particular it promotes marsh formation closer to the inlet while slightly reducing it more landward (Fig. 8). Decreasing the seeding rate tenfold decreases basin filling, similar to the effect of an initial deeper bathymetry.

4. Discussion

4.1 Marsh dynamics

The model successfully reproduced the filling of the basin and the formation of marshes in the last 2500 years. Most notably is perhaps the irregularity of marsh growth (Fig. 2, 3B, video 1), even in the presence of a constant RLSR rate and mud supply. Specifically, large (~1 km^2) swaths of marsh are created within a century (e.g., those formed between year 1000 and 1500).

The results conform to the idea of the three phases of marsh development (Xu et al., 2022): preparation, encroachment, and adjustment. In our case, preparation entails the formation of sand bars and the accumulation of mud at the edge of the basin. Encroachments entails vegetation seeding of recently deposited beds, as well as lateral expansion of recently formed vegetation patches. Adjustment entails the gradual adjustment toward a dynamic vertical equilibrium (e.g., the fast vertical accretion of the marsh formed around year 2500). Contrary to (Xu et al., 2022), however, our models suggest that these phases take place over hundreds of years as opposed to tens of years. This might be explained by the presence of waves – not present in (Xu et al., 2022) – which drastically slow down mud accumulation as well as vegetation colonization.

4.2 When does a basin fill in with marshes?

The models agrees with the hypothesis that the balance between marsh progradation and retreat is controlled by external mud supply (Mariotti and Canestrelli, 2017; Mariotti and Fagherazzi, 2010; Willemsen et al., 2022) (Fig. 5). A large enough mud supply allows the formation of shallow mud deposits at the edge of the basin, which are eventually colonized by vegetation and lead to marsh progradation.

The model suggests that Barnstable has been slowly filling with marshes in up to present time – the same conclusion reached based on the stratigraphy measurements alone (Redfield, 1972). The presence of present-day marsh expansion is at odds with the recent trend of marsh loss, including in New England marshes (Watson et al., 2016). This might be explained by a slightly larger mud supply in the nearshore than on other areas in New England – perhaps the lower portion of Cape Cod Bay (Fig. 1) accumulates some of the mud resuspended in the more swell exposed shelf on the north.

The role of initial bathymetry in shaping the evolution of a basin has been previously identified (van Maanen et al., 2013; Zhou et al., 2014). A deeper bathymetry requires more sediment to fill in. This suggest that, for a given mud supply, not only the initial size (Mariotti and Fagherazzi, 2013) but also the initial depth controls whether a basin fills in, fills in partly, or remains nearly devoid of marshes. Overall, the dependence on the initial basin size and depth might explain why Plymouth Bay – a larger basin located ~50 km north of Barnstable (Fig. 1A) – is mostly devoid of marshes.

4.3 Sensitivity to erosion and vegetation processes

As previously concluded (Elmilady et al., 2019), locally generated waves within the basin are a fundamental mechanism, especially when the basin is initially empty. Their effect would be negligible only when the whole basin is filled with marshes (e.g., Fig. 6), or when the basin is small to start with (e.g., shorter than 1 km).

Marsh edge erodibility is a relatively minor factor in the marsh trajectory (Fig. 7), likely because of the relatively small fetches and relatively low marsh edge erodibility. On the other hand, the marsh trajectory is strongly affected by wave-driven resuspension of the bed sediments (Fig. 7). Indeed, large sediment resuspension – by either stronger wind or more mud erosion (Fig. 7) – reduces the accumulation of mud at the basin edges and hence its colonization by vegetation. Mud resuspension also depends on other parameters, such as critical bed shear stress (τ_{cr}), mud erodibility rate (m_e), bed roughness (d_o), and mud settling velocity (w_m). Even though each parameter was not calibrated individually, the realistic model results at both long (Fig. 3) and short (Fig. 4) time scales indicate that the combination of the chosen parameters was appropriate.

Of the factors affecting mud resuspension (Fig. 7), the sensitivity to wind speed is possibly the most striking. Variations in wind speed on the order of 10%, which might be expected when considering different marsh settings worldwide, determine whether the basin nearly fills of barely fills with marshes. Therefore, changing meteorologic conditions may be an underappreciated control on marsh trajectory.

Vegetation dynamics also affects the marsh trajectory, but not as much as the sediment parameters. Increasing the seeding rate does not accelerate marsh expansion (Fig. 8), indicating that it is not a limiting factor. In this case the limiting factor is the development of suitable shallow area, i.e., the preparation phase (Xu et al., 2022). If the seeding rate is largely reduced, however, it can become a limiting factor and reduce the overall marsh expansion.

4.4 Model limitations

The model does not recreate realistic sandy channels in the seaward portion of the tidal flat, where channels are fewer and larger than the real ones (Fig. 2). This is probably a consequence of the symmetrical tidal flow (ebb and flood). In reality, ebb and tidal flow currents take different routes, which promotes the formation of mutually evasive channels and shoals (van Veen et al., 2005). Hence, the results in the areas closer to the inlet should be considered less reliable.

The model is also limited by the highly simplified connection with the nearshore, and the imposed sediment concentration at the inlet. For example, the tidal inlet is mostly static, whereas in reality is highly mobile mostly due to rapid morphodynamic changes in the nearshore and the ebb tidal deltas.

The model is also limited by the assumption of a single sand grain size. Field measurements indicate that the grain size is two to four times coarser in the inlet area than in the inside of the basin (Redfield, 1972). Such coarser sand likely explains the presence of shallower – and thus wider and more numerous – channels in this area than reproduced by the model. Even though this could be technically included in the model, it does not seem essential to reproduce the marsh dynamics.

The model does not keep track of organic matter, which is instead merged with the mud fraction. This can also be addressed by including an additional sediment class, even though it is still limited by poor knowledge of the fate (e.g., rate of decomposition) of the eroded organic matter.

4.5 Future predictions

After calibration, the model can be used to make predictions about the future marsh evolution. Although many climatic scenarios can be considered, here we focus on just two: one where RSLR rate remains the same as the last century (3 mm/yr), and one where it increases to 10 mm/yr.

Barnstable was on a trajectory to completely fill in, but an increase in RSLR rate halts this trend (i.e., shuts down new marsh expansion) and also triggers net marsh retreat (Fig. 9). Even in the highest RSLR scenario, however, marsh edge retreat is relatively small, on the order of 0.1-0.3 m/yr in the most exposed areas. These rates are consistent with those measured in New England salt marshes exposed to large waves. The low rates are caused by the restricted fetch in the present-day configuration (at most 2 km), and by the low marsh edge erodibility.

The marsh platform loses up to 1 m of elevation after 200 years in the highest RSLR scenario; the whole high marsh transition to low marsh, as predicted by previous models (Alizad et al., 2022; Langston et al., 2020). Nonetheless, the marsh does not drown. Given that the maximum in situ organic accretion is 5 mm/yr, this reflects the availability of sediment due to the reworking of the tidal flats and the tidal channels, an effect not simulated by models that assume a fixed bathymetry (Alizad et al., 2022; Langston et al., 2020). Indeed, the marsh has a high capacity to accrete by mud deposition when its elevation is low (Figs. 4B, 10). Furthermore, the high sediment supply prevents the ponds from entering the runaway trajectory (Mariotti, 2016).

The lowering of the marsh platform increases the tidal prism; this then causes widening of the marsh channels as previously predicted (Mariotti, 2020). Noteworthy, widening of channels is widespread in New England marshes (Mariotti, 2018; Smith, 2024; Watson et al., 2016), and might constitute the dominant mechanism of marsh loss in mesotidal marshes (Mariotti, 2020).

5. Conclusions

The improved MarshMorpho2D includes all the key processes previously identified as necessary to reproduce a realistic long-term marsh morphodynamic trajectory. In particular, the model includes vegetation population dynamics as in recently developed models, but it is less numerically expensive. Therefore, the novelty of the model does not reside in any particular new process, but rather in the ability to include all the processes in a long-term (2500 year) simulation, and to successfully hindcast the whole trajectory of a real marsh site.

This study confirms the dependence of marsh morphodynamics on previously identified factors: initial bathymetry, mud supply from the nearshore, wind and wave erosion parameters, and vegetation parameters. Each one of these factors is important yet difficult to calibrate on its own. Matching the long-term evolution with the stratigraphic record provides a global constraint for the processes and parameters in the model, increasing the confidence in future long-term predictions. We suggest that this should become a complementary approach to calibrate and validate marsh evolution models.

The newly calibrated model can be used to predict with more confidence the future marsh evolution, fully including the morphodynamics feedback associated with evolving channels and tidal flats. For the Barnstable marsh, the model indicates that the marsh will lower its elevation for a high RSLR rate scenario, but it will not drown even after 200 years, likely because of sediment recycling from eroding channels and tidal flat. On the other hand, major marsh loss will occur due to channel widening and, in minor part, wave-driven edge erosion. The model could be further used to address the effect of marsh restoration activities, such as marsh edge protection, thin-layer placement, and new marsh creation.

Acknowledgements

This work was funded by the US Coastal Research Program through the US Army Engineer Research and Development Center, award #W912HZ2020029. The code is available at https://csdms.colorado.edu/wiki/Model:MarshMorpho2D.

Table 1. Parameters used in the model.

Vegetation dynamics		
v_{growth}	Vegetation growth rate	1 year^{-1}
v_{seed}	Vegetation seeding rate	0.02 year^{-1}
$v_{expansion}$	Vegetation lateral expansion rate	1 m/yr
	Flow mortality bed shear stress	0.2 Pa
R_{org}	Maximum in situ organic accretion	5 mm/yr
Hydrodynamics		
r	Tidal range (low, middle, high)	2.21, 2.87, 3.63 m

sla	Sea level anomaly (low, middle, high)	-0.14, 0, 0.13 m
T	Tidal period	12.4 hours
n (unvegetated)	Manning coefficient	0.05 $m^{1/3}/s$
n (vegetated)	Manning coefficient	0.1 $m^{1/3}/s$
Sediment dynamics		
w_M	Mud settling velocity	0.2 mm/s
w_s	Sand settling velocity	20 mm/s
d_{50}	Sand median grain size	0.25 mm
τ_{cr}	Critical shear stress for mud erosion	0.2 Pa
m_e	Mud erodibility rate	1.5 10^{-5} $kg/m^2/s$
k (sand)	Coefficient for tidal dispersion	0.5
k (mud)	Coefficient for tidal dispersion	0.1
Ko (sand)	Baseline sand diffusivity	0
Ko (mud, unvegetated)	Baseline mud diffusivity	10 m^2/s
Ko (mud, vegetated)	Baseline mud diffusivity	0.1 m^2/s
a_{edge}	Wave edge erosion rate	0.01 m/yr/(W/m)

Figure 1. A) Location of Barnstable marsh (Massachusetts, USA). B) Aerial image (3/11/2012) Landsat/Copernicus, retrieved with GoogleEarth. C) Historical map from 1788 (Des Barres, 1780). The red ellipses indicate a marsh area that formed after 1780 a.d.

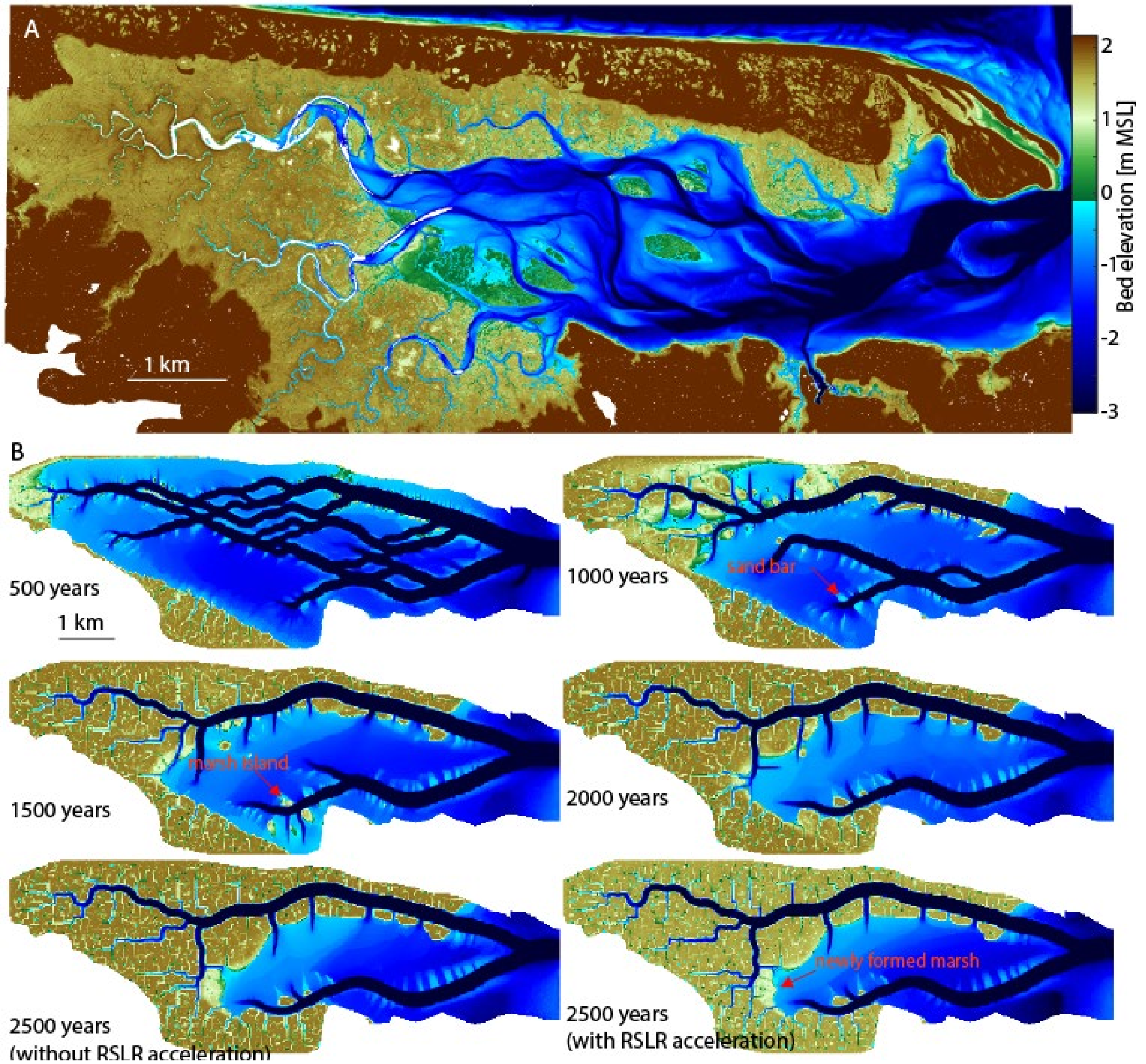

Figure 2. A) Topobathymetry from year 2018 (NOAA). Note the white areas in the channel on the west side indicate the lack of data (deep channels not captured by the Lidar). B) Modeled marsh evolution, showing the topobathymetry at different times. Year 2500 is assumed to be equal to present-day (about year 2000 a.d.). The last two panels show the simulations with and without RSLR acceleration from 0.7 to 3 mm/yr starting at year 2400.

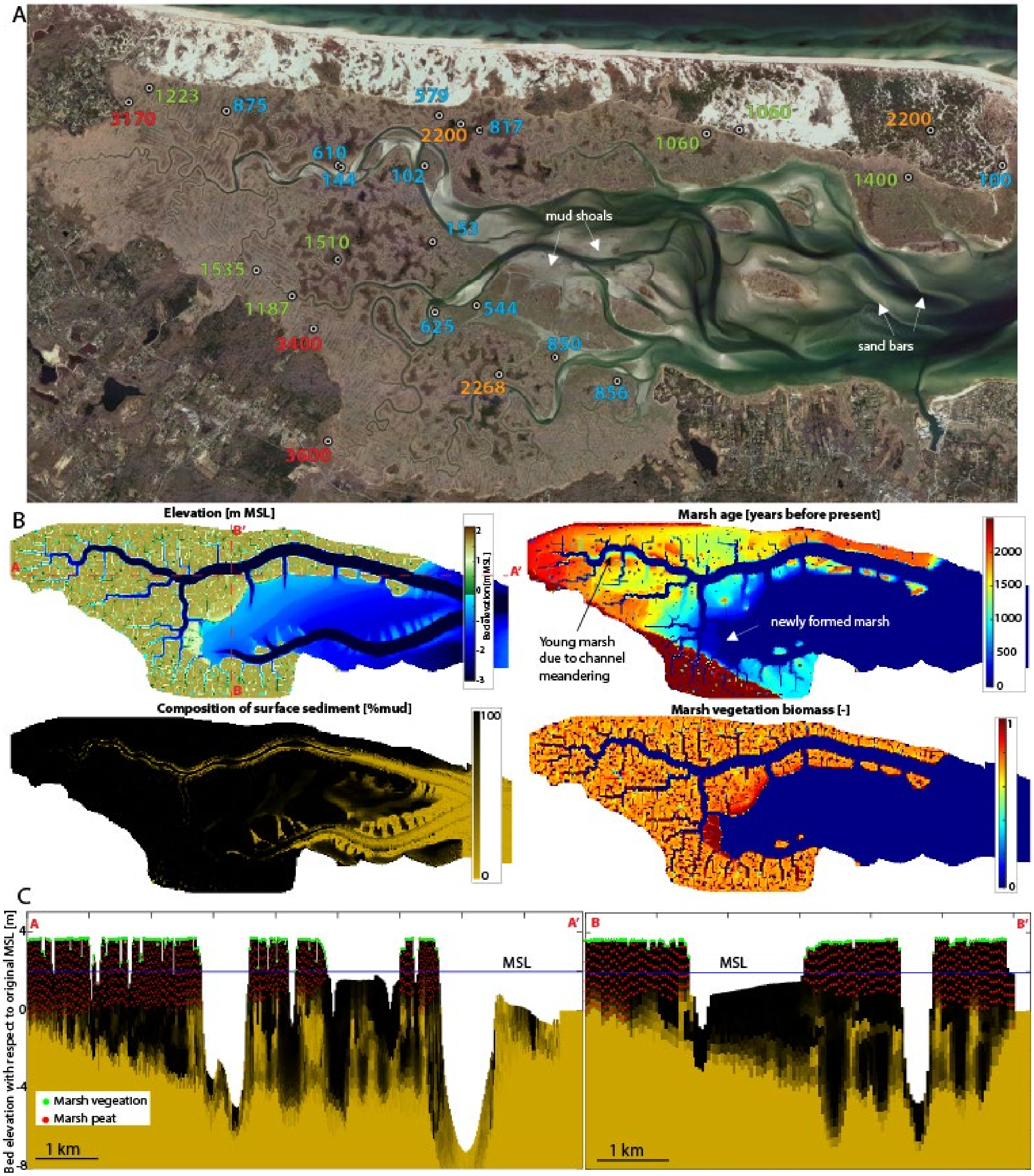

Figure 3. A) Marsh dates (reported in years before present) are from (Braswell et al., 2020), and are color-coded by millennia. B) Model results at year 2500: topobathymetry, marsh age, surface sediment composition, vegetation biomass. C) Model results at year 2500: stratigraphy cross section along and across the basin, also showing the presence of marsh peat (vegetated cells that got buried).

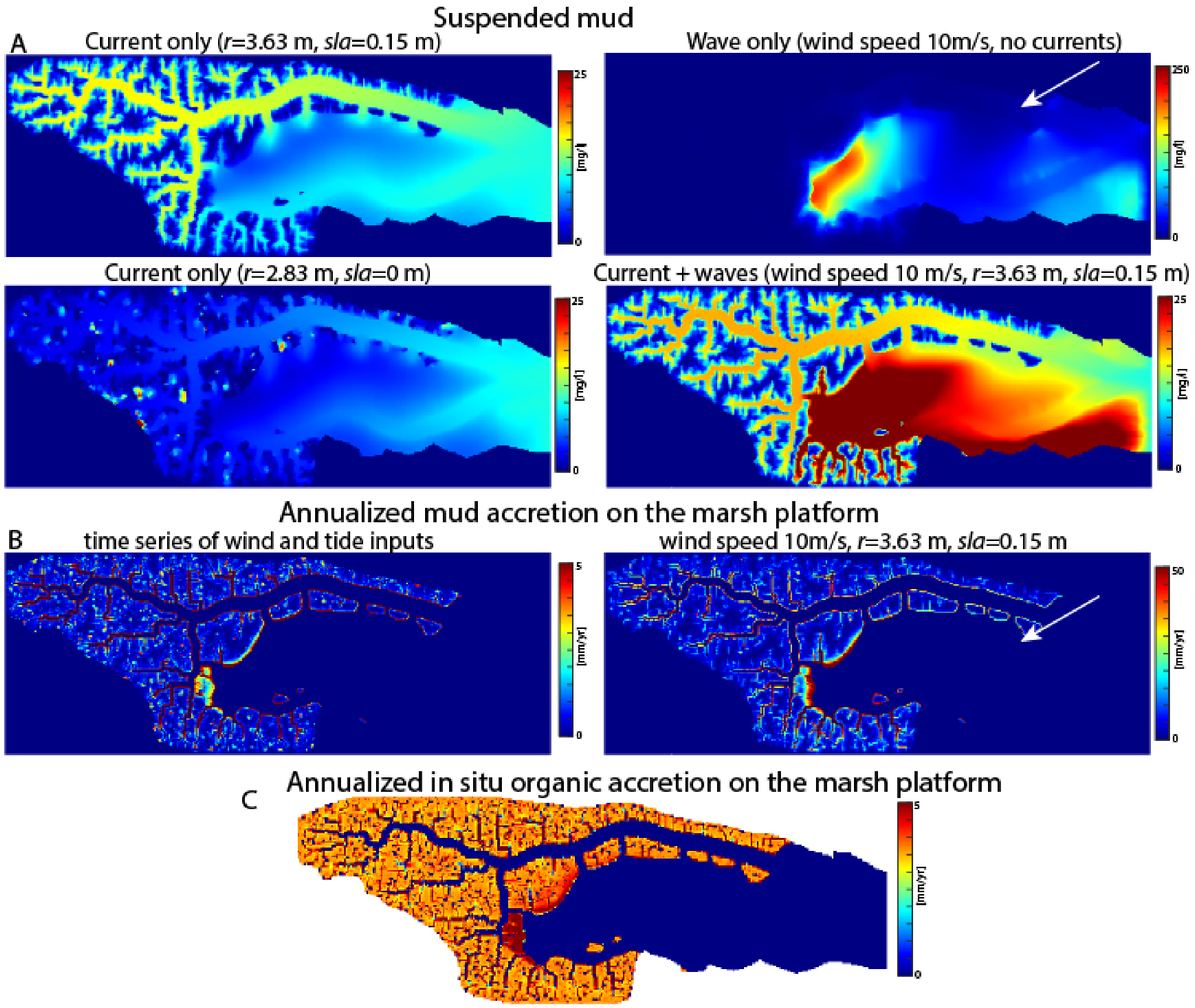

Figure 4. A) Map of suspended mud, calculated with the topobathymetry at year 2500 with selected hydrodynamic forcings. B) Annualized mud deposition on the marsh. C) Annualized in situ organic accretion on the marsh.

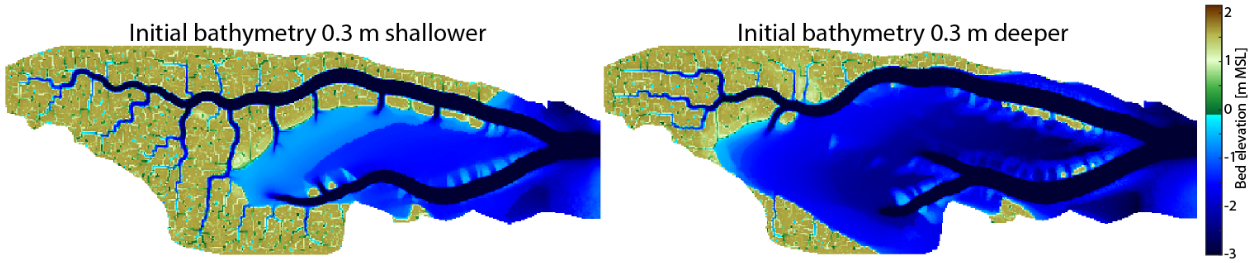

Figure 5. Sensitivity to initial basin depth, comparing the topobathymetry at year 2500.

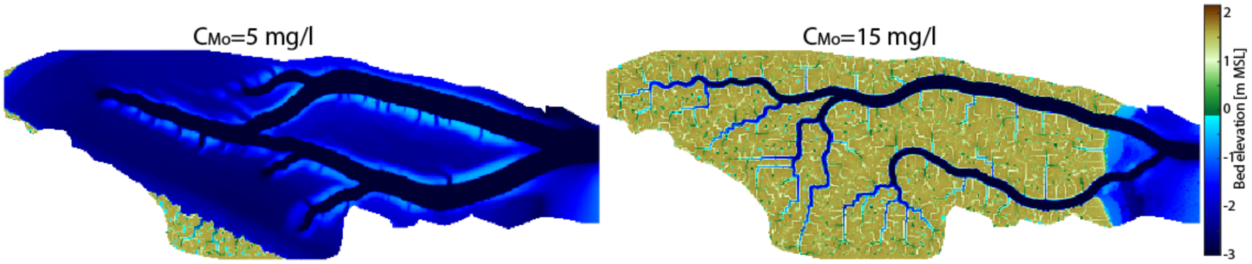

Figure 6. Sensitivity to mud sediment concentration at the inlet (c_{Mo}), comparing the topobathymetry at year 2500.

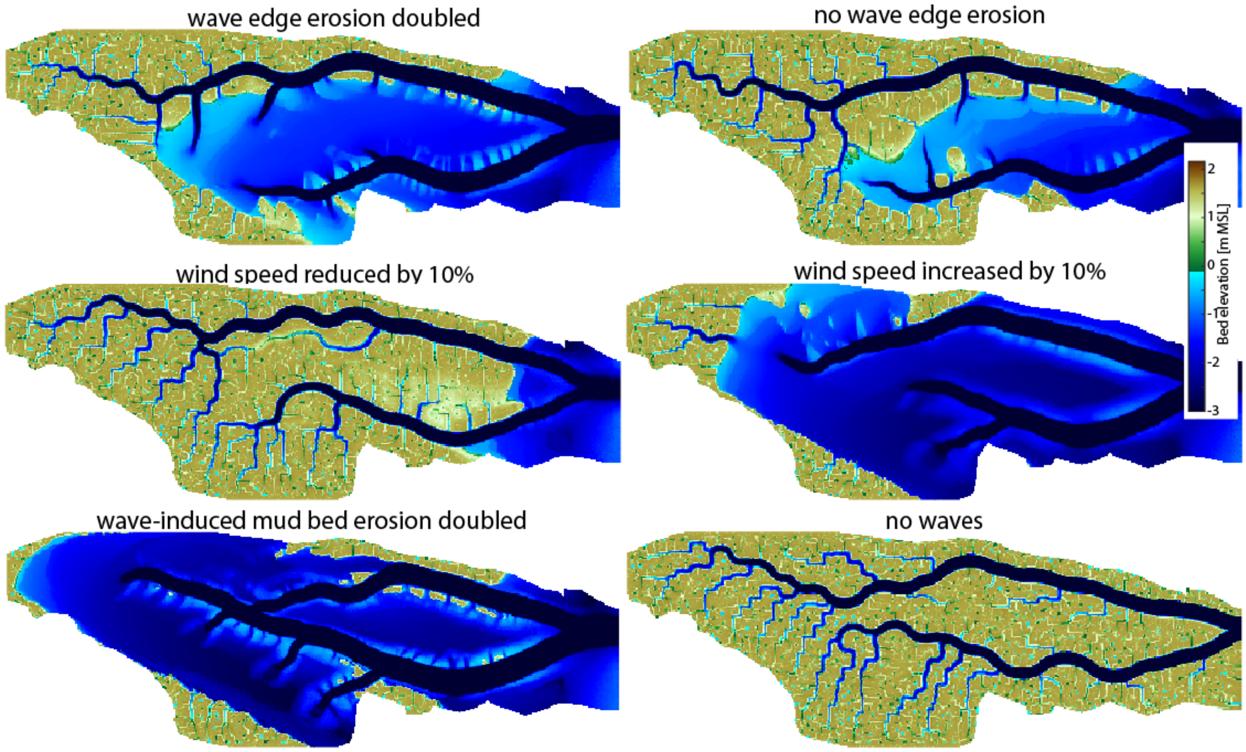

Figure 7. Sensitivity to wind and wave-related processes, comparing the topobathymetry at year 2500.

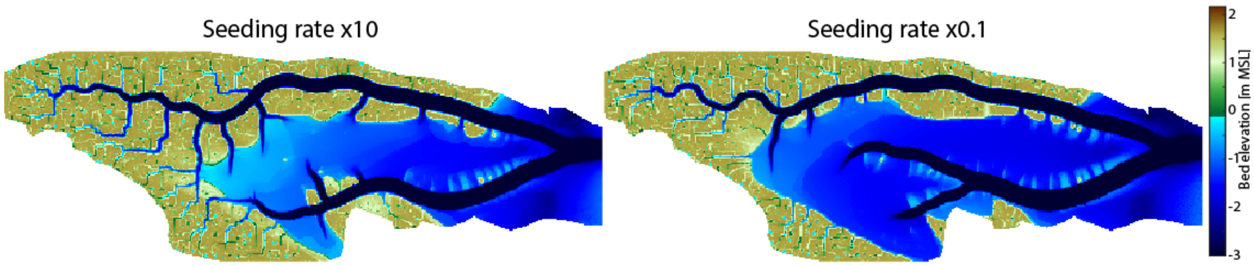

Figure 8. Sensitivity to vegetation dynamics, comparing the topobathymetry at year 2500.

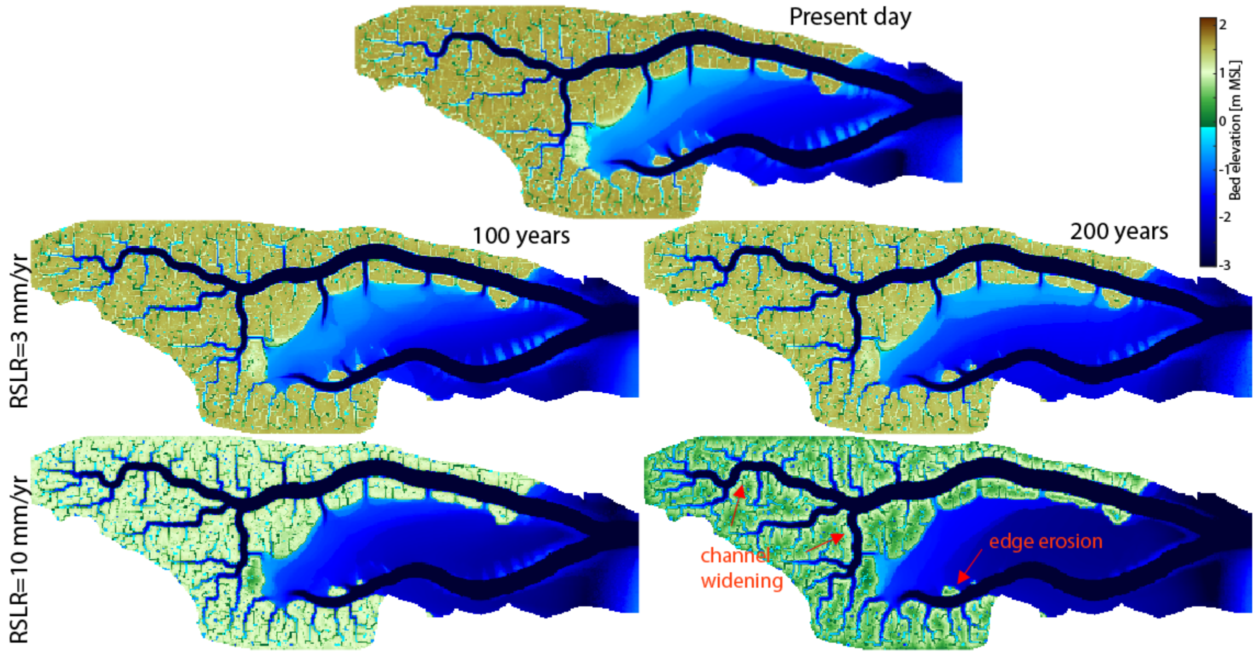

Figure 9. Model predictions with different rates of RSLR, starting from the modeled present-day condition.

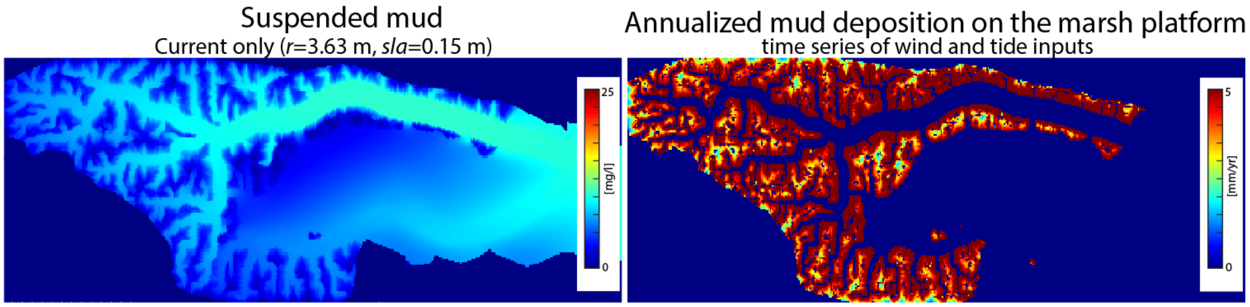

Figure 10. Suspended mud from currents and annualized mud accretion (as in Fig. 4A,B) calculated based on the topobathymetry 200 years after present-day with a RLSR rate of 10 mm/yr (Fig. 9). Note that for the same tide (*r*=3.63 m, *sla*=0.15 m), the suspended mud on the marsh platform is higher compared to the present-day topobathymetry (Fig. 4A).

References

Alizad, K., Hagen, S.C., Morris, J.T., Bacopoulos, P., Bilskie, M.V., Weishampel, J.F., Medeiros, S.C., 2016. A coupled, two-dimensional hydrodynamic-marsh model with biological feedback. Ecol. Model. 327, 29–43. https://doi.org/10.1016/j.ecolmodel.2016.01.013

Alizad, K., Morris, J.T., Bilskie, M.V., Passeri, D.L., Hagen, S.C., 2022. Integrated Modeling of Dynamic Marsh Feedbacks and Evolution Under Sea-Level Rise in a Mesotidal Estuary (Plum Island, MA, USA). Water Resour. Res. 58, e2022WR032225. https://doi.org/10.1029/2022WR032225

Baranes, H.E., Woodruff, J.D., Geyer, W.R., Yellen, B.C., Richardson, J.B., Griswold, F., 2022. Sources, Mechanisms, and Timescales of Sediment Delivery to a New England Salt Marsh. J. Geophys. Res. Earth Surf. 127, e2021JF006478. https://doi.org/10.1029/2021JF006478

Boechat Albernaz, M., Brückner, M.Z.M., van Maanen, B., van der Spek, A.J.F., Kleinhans, M.G., 2023. Vegetation Reconfigures Barrier Coasts and Affects Tidal Basin Infilling Under Sea Level Rise. J. Geophys. Res. Earth Surf. 128, e2022JF006703. https://doi.org/10.1029/2022JF006703

Braswell, A.E., Heffernan, J.B., Kirwan, M.L., 2020. How Old Are Marshes on the East Coast, USA? Complex Patterns in Wetland Age Within and Among Regions. Geophys. Res. Lett. 47, e2020GL089415. https://doi.org/10.1029/2020GL089415

Bromberg, K.D., Bertness, M.D., 2005. Reconstructing New England salt marsh losses using historical maps. Estuaries 28, 823–832. https://doi.org/10.1007/BF02696012

Brückner, M.Z.M., Schwarz, C., van Dijk, W.M., van Oorschot, M., Douma, H., Kleinhans, M.G., 2019. Salt Marsh Establishment and Eco-Engineering Effects in Dynamic Estuaries Determined by Species Growth and Mortality. J. Geophys. Res. Earth Surf. 124, 2962–2986. https://doi.org/10.1029/2019JF005092

Burns, C.J., Alexander, C.R., Alber, M., 2020. Assessing Long-Term Trends in Lateral Salt-Marsh Shoreline Change along a U.S. East Coast Latitudinal Gradient. J. Coast. Res. 37, 291–301. https://doi.org/10.2112/JCOASTRES-D-19-00043.1

Cahoon, D.R., Lynch, J.C., Roman, C.T., Schmit, J.P., Skidds, D.E., 2019. Evaluating the Relationship Among Wetland Vertical Development, Elevation Capital, Sea-Level Rise, and Tidal Marsh Sustainability. Estuaries Coasts 42, 1–15. https://doi.org/10.1007/s12237-018-0448-x

Cao, H., Zhu, Z., Herman, P.M.J., Temmerman, S., de Smit, J., Zhang, L., Yuan, L., Bouma, T.J., 2021. Plant traits determining biogeomorphic landscape dynamics: A study on clonal expansion strategies driving cliff formation at marsh edges. Limnol. Oceanogr. 66, 3754–3767. https://doi.org/10.1002/lno.11915

Carniello, L., Defina, A., D'Alpaos, L., 2012. Modeling sand-mud transport induced by tidal currents and wind waves in shallow microtidal basins: Application to the Venice Lagoon (Italy). Estuar. Coast. Shelf Sci. 102–103, 105–115. https://doi.org/10.1016/j.ecss.2012.03.016

Carniello, L., Defina, A., D'Alpaos, L., 2009. Morphological evolution of the Venice lagoon: Evidence from the past and trend for the future. J. Geophys. Res. Earth Surf. 114, F04002. https://doi.org/10.1029/2008JF001157

Coleman, D.J., Ganju, N.K., Kirwan, M.L., 2020. Sediment Delivery to a Tidal Marsh Platform Is Minimized by Source Decoupling and Flux Convergence. J. Geophys. Res. Earth Surf. 125, e2020JF005558. https://doi.org/10.1029/2020JF005558

Coleman, D.J., Schuerch, M., Temmerman, S., Guntenspergen, G., Smith, C.G., Kirwan, M.L., 2022. Reconciling models and measurements of marsh vulnerability to sea level rise. Limnol. Oceanogr. Lett. n/a. https://doi.org/10.1002/lol2.10230

Colina Alonso, A., van Maren, D.S., van Weerdenburg, R.J.A., Huismans, Y., Wang, Z.B., 2023. Morphodynamic Modeling of Tidal Basins: The Role of Sand-Mud Interaction. J. Geophys. Res. Earth Surf. 128, e2023JF007391. https://doi.org/10.1029/2023JF007391

Craft, C., Clough, J., Ehman, J., Joye, S., Park, R., Pennings, S., Guo, H., Machmuller, M., 2009. Forecasting the effects of accelerated sea-level rise on tidal marsh ecosystem services. Front. Ecol. Environ. 7, 73–78. https://doi.org/10.1890/070219

Crosby, S.C., Sax, D.F., Palmer, M.E., Booth, H.S., Deegan, L.A., Bertness, M.D., Leslie, H.M., 2016. Salt marsh persistence is threatened by predicted sea-level rise. Estuar. Coast. Shelf Sci. 181, 93–99. https://doi.org/10.1016/j.ecss.2016.08.018

D'Alpaos, A., Da Lio, C., Marani, M., 2012. Biogeomorphology of tidal landforms: physical and biological processes shaping the tidal landscape. Ecohydrology 5, 550–562. https://doi.org/10.1002/eco.279

Dam, G., van der Wegen, M., Labeur, R.J., Roelvink, D., 2016. Modeling centuries of estuarine morphodynamics in the Western Scheldt estuary. Geophys. Res. Lett. 43, 3839–3847. https://doi.org/10.1002/2015GL066725

Des Barres, J.F.W., 1780. A chart of the coast of New York, New Jersey, Pennsilvania, Maryland, Virginia, North Carolina. Atl. Neptune.

Di Silvio, G., Dall'Angelo, C., Bonaldo, D., Fasolato, G., 2010. Long-term model of planimetric and bathymetric evolution of a tidal lagoon. Cont. Shelf Res., The Coastal Morphodynamics of Venice Lagoon and its Inlets 30, 894–903. https://doi.org/10.1016/j.csr.2009.09.010

Doar, William R., Luciano, K.E., 2023. Quantifying Multi-Decadal Salt Marsh Surface Elevation and Geodetic Change: The South Carolina Geological Survey SET Network. Estuaries Coasts. https://doi.org/10.1007/s12237-023-01290-y

Elmilady, H., van der Wegen, M., Roelvink, D., Jaffe, B.E., 2019. Intertidal Area Disappears Under Sea Level Rise: 250 Years of Morphodynamic Modeling in San Pablo Bay, California. J. Geophys. Res. Earth Surf. 124, 38–59. https://doi.org/10.1029/2018JF004857

Elsey-Quirk, T., Mariotti, G., Valentine, K., Raper, K., 2019. Retreating marsh shoreline creates hotspots of high-marsh plant diversity. Sci. Rep. 9, 5795. https://doi.org/10.1038/s41598-019-42119-8

Fagherazzi, S., Mariotti, G., 2012. Mudflat runnels: Evidence and importance of very shallow flows in intertidal morphodynamics. Geophys. Res. Lett. 39. https://doi.org/10.1029/2012GL052542

Fagherazzi, S., Viggato, T., Vieillard, A.M., Mariotti, G., Fulweiler, R.W., 2017. The effect of evaporation on the erodibility of mudflats in a mesotidal estuary. Estuar. Coast. Shelf Sci. 194, 118–127. https://doi.org/10.1016/j.ecss.2017.06.011

Gourgue, O., van Belzen, J., Schwarz, C., Vandenbruwaene, W., Vanlede, J., Belliard, J.-P., Fagherazzi, S., Bouma, T.J., van de Koppel, J., Temmerman, S., 2021. Biogeomorphic modeling to assess resilience of tidal marsh restoration to sea level rise and sediment supply. Earth Surf. Dyn. Discuss. 1–38. https://doi.org/10.5194/esurf-2021-66

Gunnell, J.R., Rodriguez, A.B., McKee, B.A., 2013. How a marsh is built from the bottom up. Geology 41, 859–862. https://doi.org/10.1130/G34582.1

Hein, Fitzgerald, Barnhardt, W.A., Stone, B., 2010. Onshore-Offshore Surficial Geologic Map of the Newburyport East and Northern Half of the Ipswich Quadrangles, Massachusetts [WWW Document].

Houttuijn Bloemendaal, L.J., FitzGerald, D.M., Hughes, Z.J., Novak, A.B., Phippen, P., 2021. What controls marsh edge erosion? Geomorphology 386, 107745. https://doi.org/10.1016/j.geomorph.2021.107745

Jafari, N.H., Harris, B.D., Cadigan, J.A., Day, J.W., Sasser, C.E., Kemp, G.P., Wigand, C., Freeman, A., Sharp, L.A., Pahl, J., Shaffer, G.P., Holm, G.O., Lane, R.R., 2019. Wetland shear strength with emphasis on the impact of nutrients, sediments, and sea level rise. Estuar. Coast. Shelf Sci. 229, 106394. https://doi.org/10.1016/j.ecss.2019.106394

Jankowski, K.L., Törnqvist, T.E., Fernandes, A.M., 2017. Vulnerability of Louisiana's coastal wetlands to present-day rates of relative sea-level rise. Nat. Commun. 8, 14792. https://doi.org/10.1038/ncomms14792

Kirwan, M.L., Murray, A.B., 2012. Rapid wetland expansion during European settlement and its implication for marsh survival under modern sediment delivery rates: REPLY. Geology 40, e286–e286. https://doi.org/10.1130/G33827Y.1

Langston, A.K., Durán Vinent, O., Herbert, E.R., Kirwan, M.L., 2020. Modeling long-term salt marsh response to sea level rise in the sediment-deficient Plum Island Estuary, MA. Limnol. Oceanogr. 65, 2142–2157. https://doi.org/10.1002/lno.11444

Le Hir, P., Cayocca, F., Waeles, B., 2011. Dynamics of sand and mud mixtures: A multiprocess-based modelling strategy. Cont. Shelf Res., Proceedings of the 9th International Conference on Nearshore and Estuarine Cohesive Sediment Transport Processes 31, S135–S149. https://doi.org/10.1016/j.csr.2010.12.009

Mariotti, Canestrelli, A., 2017. Long-term morphodynamics of muddy backbarrier basins: Fill in or empty out? Water Resour. Res. 53, 7029–7054. https://doi.org/10.1002/2017WR020461

Mariotti, G., 2021. Self-organization of coastal barrier systems during the Holocene. J. Geophys. Res.-Earth Surf.

Mariotti, G., 2020. Beyond marsh drowning: The many faces of marsh loss (and gain). Adv. Water Resour. 144, 103710. https://doi.org/10.1016/j.advwatres.2020.103710

Mariotti, G., 2018. Marsh channel morphological response to sea level rise and sediment supply. Estuar. Coast. Shelf Sci. 209, 89–101. https://doi.org/10.1016/j.ecss.2018.05.016

Mariotti, G., 2016. Revisiting salt marsh resilience to sea level rise: Are ponds responsible for permanent land loss? J. Geophys. Res. Earth Surf. 121, 1391–1407. https://doi.org/10.1002/2016JF003900

Mariotti, G., Fagherazzi, S., 2013. Critical width of tidal flats triggers marsh collapse in the absence of sea-level rise. Proc. Natl. Acad. Sci. 110, 5353–5356. https://doi.org/10.1073/pnas.1219600110

Mariotti, G., Fagherazzi, S., 2010. A numerical model for the coupled long-term evolution of salt marshes and tidal flats. J. Geophys. Res. Earth Surf. 115. https://doi.org/10.1029/2009JF001326

Mariotti, G., Finotello, A., 2024. A flow-curvature-based model for channel meandering in tidal marshes. Water Resour. Res. in press.

Mariotti, G., Spivak, A.C., Luk, S.Y., Ceccherini, G., Tyrrell, M., Gonneea, M.E., 2020. Modeling the spatial dynamics of marsh ponds in New England salt marshes. Geomorphology 365, 107262. https://doi.org/10.1016/j.geomorph.2020.107262

Mariotti, G., Zapp, S., 2022. A framework to simplify astro-meteorological water levels and wind inputs for coastal marsh ecomorphodynamics. JGR - Earth Surf.

Mariotti, Huang, H., Xue, Z., Li, B., Justic, D., Zang, Z., 2018. Biased Wind Measurements in Estuarine Waters. J. Geophys. Res. Oceans 123, 3577–3587. https://doi.org/10.1029/2017JC013748

Morris, J.T., Sundareshwar, P.V., Nietch, C.T., Kjerfve, B., Cahoon, D.R., 2002. Responses of coastal wetlands to rising sea level. Ecology 83, 2869–2877. https://doi.org/10.2307/3072022

Nolte, S., Koppenaal, E.C., Esselink, P., Dijkema, K.S., Schuerch, M., De Groot, A.V., Bakker, J.P., Temmerman, S., 2013. Measuring sedimentation in tidal marshes: a review on methods and their applicability in biogeomorphological studies. J. Coast. Conserv. 17, 301–325. https://doi.org/10.1007/s11852-013-0238-3

Ortiz, A.C., Ashton, A.D., 2016. Exploring shoreface dynamics and a mechanistic explanation for a morphodynamic depth of closure. J. Geophys. Res. Earth Surf. 121, 442–464. https://doi.org/10.1002/2015JF003699

Priestas, A.M., Fagherazzi, S., Wilson, C.A., FitzGerald, D.M., 2012. Rapid wetland expansion during European settlement and its implication for marsh survival under modern sediment delivery rates: COMMENT. Geology 40, e284–e285. https://doi.org/10.1130/G32597C.1

Redfield, A.C., 1972. Development of a New England Salt Marsh. Ecol. Monogr. 42, 201–237. https://doi.org/10.2307/1942263

Redfield, A.C., 1965. Ontogeny of a Salt Marsh Estuary. Science 147, 50–55. https://doi.org/10.1126/science.147.3653.50

Schrijvershof, R., Maren, B. van, Vermeulen, B., Hoitink, T., 2021. Intertidal floodplain controls on centennial-scale morphological channel development (No. EGU21-16435). Presented at the EGU21, Copernicus Meetings. https://doi.org/10.5194/egusphere-egu21-16435

Smith, S., 2024. The effects of Sesarma reticulatum (L.) herbivory and sea level rise on creek expansion in Cape Cod salt marshes. Cont. Shelf Res. 272, 105146. https://doi.org/10.1016/j.csr.2023.105146

Swart, D.H., 1974. Offshore sediment transport and equilibrium profiles,. Delft Hydraul. Lab. 131, 1–217.

Törnqvist, T.E., Cahoon, D.R., Morris, J.T., Day, J.W., 2021. Coastal Wetland Resilience, Accelerated Sea-Level Rise, and the Importance of Timescale. AGU Adv. 2, e2020AV000334. https://doi.org/10.1029/2020AV000334

Törnqvist, T.E., Jankowski, K.L., Li, Y.-X., González, J.L., 2020. Tipping points of Mississippi Delta marshes due to accelerated sea-level rise. Sci. Adv. 6, eaaz5512. https://doi.org/10.1126/sciadv.aaz5512

Valentine, K., Mariotti, G., 2019. Wind-driven water level fluctuations drive marsh edge erosion variability in microtidal coastal bays. Cont. Shelf Res. 176, 76–89. https://doi.org/10.1016/j.csr.2019.03.002

van de Vijsel, R.C., van Belzen, J., Bouma, T.J., van der Wal, D., Borsje, B.W., Temmerman, S., Cornacchia, L., Gourgue, O., van de Koppel, J., 2023. Vegetation controls on channel network complexity in coastal wetlands. Nat. Commun. 14, 7158. https://doi.org/10.1038/s41467-023-42731-3

Van Der Wegen, M., Reyns, J., Jaffe, B., Foxgrover, A., Achete, F., Marvin-Dipasquale, M., Fregoso, T., Nam, J., Lovering, J., 2023. Successful hindcast of 7 years of mud morphodynamics influenced by salt pond restoration in south san francisco bay, in: Coastal Sediments 2023. WORLD SCIENTIFIC, pp. 1129–1134. https://doi.org/10.1142/9789811275135_0103

van der Wegen, M., Roelvink, J.A., 2012. Reproduction of estuarine bathymetry by means of a process-based model: Western Scheldt case study, the Netherlands. Geomorphology 179, 152–167. https://doi.org/10.1016/j.geomorph.2012.08.007

van Heteren, S., van de Plassche, O., 1997. Influence of relative sea-level change and tidal-inlet development on barrier-spit stratigraphy, Sandy Neck, Massachusetts. J. Sediment. Res. 67, 350–363. https://doi.org/10.1306/D426856D-2B26-11D7-8648000102C1865D

van Ledden, M., van Kesteren, W.G.M., Winterwerp, J.C., 2004. A conceptual framework for the erosion behaviour of sand–mud mixtures. Cont. Shelf Res. 24, 1–11. https://doi.org/10.1016/j.csr.2003.09.002

van Maanen, B., Coco, G., Bryan, K.R., 2013. Modelling the effects of tidal range and initial bathymetry on the morphological evolution of tidal embayments. Geomorphology 191, 23–34. https://doi.org/10.1016/j.geomorph.2013.02.023

van Veen, J., van der Spek, A.J.F., Stive, M.J.F., Zitman, T., 2005. Ebb and flood channel systems in the Netherlands tidal waters. J. Coast. Res. 21, 1107–1120. https://doi.org/10.2112/04-0394.1

Watson, E., Raposa, K., Carey, J., Wigand, C., Warren, R., 2016. Anthropocene Survival of Southern New England’s Salt Marshes. Estuaries Coasts DOI10.1007/s12237-016-0166-1. https://doi.org/10.1007/s12237-016-0166-1

Wiberg, P.L., Sherwood, C.R., 2008. Calculating wave-generated bottom orbital velocities from surface-wave parameters. Comput. Geosci. 34, 1243–1262. https://doi.org/10.1016/j.cageo.2008.02.010

Willemsen, P., Smits, B.P., Borsje, B.W., Herman, P.M.J., Dijkstra, J.T., Bouma, T.J., Hulscher, S., 2022. Modelling decadal salt marsh development: variability of the salt marsh edge under influence of waves and sediment availability. Water Resour. Res. e2020WR028962.

Wilson, C.A., Hughes, Z.J., FitzGerald, D.M., Hopkinson, C., Valentine, V., Kolker, A.S., 2014. Saltmarsh Pool and Tidal Creek Morphodynamics: Dynamic Equilibrium of Northern Latitude Saltmarshes? Geomorphology. https://doi.org/10.1016/j.geomorph.2014.01.002

Xu, Y., Kalra, T.S., Ganju, N.K., Fagherazzi, S., 2022. Modeling the Dynamics of Salt Marsh Development in Coastal Land Reclamation. Geophys. Res. Lett. 49, e2021GL095559. https://doi.org/10.1029/2021GL095559

Yellen, B., Woodruff, J.D., Baranes, H.E., Engelhart, S.E., Geyer, W.R., Randall, N., Griswold, F.R., 2023. Salt Marsh Response to Inlet Switch-Induced Increases in Tidal Inundation. J. Geophys. Res. Earth Surf. 128, e2022JF006815. https://doi.org/10.1029/2022JF006815

Young, I.R., Verhagen, L.A., 1996. The growth of fetch limited waves in water of finite depth .1. Total energy and peak frequency. Coast. Eng. 29, 47–78.

Zapp, S.M., Mariotti, G., 2023. Frictional dissipation of tidal signal exerts a significant influence on the morphological development of elongate microtidal marsh platforms, in: Coastal Sediments 2023. WORLD SCIENTIFIC, pp. 1477–1487. https://doi.org/10.1142/9789811275135_0137

Zhang, X., Fichot, C.G., Baracco, C., Guo, R., Neugebauer, S., Bengtsson, Z., Ganju, N., Fagherazzi, S., 2020. Determining the drivers of suspended sediment dynamics in tidal marsh-influenced estuaries using high-resolution ocean color remote sensing. Remote Sens. Environ. 240, 111682. https://doi.org/10.1016/j.rse.2020.111682

Zhou, Z., Coco, G., Jiménez, M., Olabarrieta, M., van der Wegen, M., Townend, I., 2014. Morphodynamics of river-influenced back-barrier tidal basins: The role of landscape and hydrodynamic settings. Water Resour. Res. 50, 9514–9535. https://doi.org/10.1002/2014WR015891